Superresolved and reference-free microparticle traction force microscopy (MP-TFM) reveals the complexity of the mechanical interaction in phagocytosis

Daan Vorselen[1,2], Yifan Wang[3], Matthew J. Footer[1,2], Wei Cai[3], Julie A. Theriot[1,2]

1 Department of Biochemistry and Howard Hughes Medical Institute, Stanford University, Stanford, CA 94305, USA

2 Department of Biology, University of Washington, Seattle, WA 98105, USA

3 Department of Mechanical Engineering, Stanford University, Stanford, CA 94305, USA

Correspondence to: jtheriot@uw.edu

Force exertion is an integral part of cellular behavior. Traction force microscopy (TFM) has been instrumental for studying such forces, providing both spatial and directional force measurements at subcellular resolution. However, the applications of classical TFM are restricted by the typical planar geometry. Here, we develop a particle-based force sensing strategy, specifically designed for studying ligand-dependent cellular interactions. We establish an accessible batch approach for synthesizing highly uniform, deformable and tunable hydrogel particles. In addition, they can be easily derivatized to trigger specific cellular behavior. The 3D shape of such particles can be resolved with superresolution (< 50 nm) accuracy using conventional confocal microscopy. We introduce a computational method that allows us to infer surface traction forces with high sensitivity (~ 10 Pa), directly from the particle shape without embedding tracers in the particle. We illustrate the potential and flexibility of this approach by measuring forces throughout phagocytic engulfment. This strategy can readily be adapted for studying cellular forces in a wide range of applications.

INTRODUCTION

Cells continuously exert forces on their environment, allowing them to probe and respond to their mechanical surroundings[1], while also engaging in interactions with neighbouring cells[2–4]. Traction force microscopy (TFM) provides the ability to study such forces in detail[5,6]. However, classical TFM is largely limited to *in vitro* applications[7], and a range of cellular processes warrant different (*i.e.* non-planar) geometries, such as cell-cell interactions like phagocytosis or the formation of the immunological synapse, in which mechanical forces have a widespread role[8,9]. Moreover, with a few notable exceptions[10–12], TFM focuses on the study of shear forces, often neglecting forces normal to the surface.

Force sensing within tissue, and *in vivo*, is a new area of exploration and first became possible by the introduction of oil droplet-based technologies[13,14]. Recently, deformable hydrogel microparticles (MPs) were also used as force reporters[15]. The use of microgels for MP based traction force microscopy (MP-TFM) shows promise for broad applicability because of the mechanical tunability over orders of magnitude and the potential to measure both shear and normal stresses. However, synthesis of suitable hydrogel MPs for such applications can be rather complex, often requiring specialized expertise in microfluidics[15,16]. Moreover, particle properties, especially their uniformity in mechanical properties, must be optimized and thoroughly characterized for accurate traction measurements[16]. Like in TFM, multiple strategies are possible for measuring deformations and for calculation of the stress fields[17], including reference-free methods[18], which have not yet been explored in MP-TFM. Finally, deformable microparticles have so far only been used as passive force reporters without biologically specific ligands, despite the fact that MPs can be chemically modified to trigger and elicit specific cellular behaviors.

Here, we describe a novel particle-based force sensing strategy, specifically designed for studying ligand-dependent cellular interactions (Supplementary Fig. 1). We established a batch production approach for synthesizing deformable tunable hydrogel particles that is simple and reproducible. The resulting particles are homogeneous throughout their volume and from particle to particle. The incorporation of carboxyl groups allows easy and efficient derivitization. Using confocal microscopy, we can

reconstruct the particle boundary with superresolution accuracy, allowing us to visualize local deformations with ~50 nm precision. Finally, we solve the inverse problem of inferring the displacement field and traction forces from the measured particle shape and traction-free regions. This is accomplished by iteratively minimizing a cost function consisting of contributions from shape mismatch, residual tractions, and the elastic energy. This procedure is enabled by a fast spherical harmonics-based method for solving the traction forces given the displacement field on a spherical surface[19]. We apply this computer-aid MP-TFM method to study the mechanical interaction of macrophages with their targets during phagocytosis.

RESULTS

Batch production of homogeneous, readily conjugatable, hydrogel microparticles with cell-like rigidity

We used membrane emulsification with Shirasu Porous Glass (SPG) membranes with uniform pore size to produce monodisperse spherical hydrogel microparticles[20,21]. Acrylamide mixtures containing monomeric acrylamide (AAm), acrylic acid (AAc) and the crosslinker N,N'-methylenebisacrylamide (BIS) were extruded through a hydrophobic SPG membrane under nitrogen pressure, generating droplets in an oil phase (Fig. 1a). After the entire aqueous mixture was dispersed, acrylamide polymerization was initiated within the droplets by addition of the free radical initiator Azobisisobutyronitrile (AIBN). The resulting deformable poly-AAm-co-AAc microparticles (DAAM-particles) were collected and resuspended in PBS. As shown previously[22,23], this strategy yields highly monodisperse particles (Fig 1b). The particle size could be tuned between 4 – 15 μm (each with coefficient of variation (CV) $\lesssim$ 0.1) using SPG membranes with various pore sizes, revealing the expected linear relation between pore and particle size[23] (Fig. 1c). Furthermore, since membrane emulsification is a bulk method, we were able to synthesize an estimated 10^{10} - 10^{11} particles per batch (Supplementary Fig. 2).

To further tune important particle properties, such as their rigidity, we changed the composition of the acrylamide mixture. In particular, the total mass concentration of acrylic compounds ($C_T = C_{AAm} + C_{AAc} + C_{BIS}$ = 100 mg/mL), as well as the relative concentration of acrylic acid ($m_{AAc}/(m_{AAm} + m_{AAc} + m_{BIS})$ = 10%) were kept constant, while the crosslinker concentration $C_c = m_{BIS}/(m_{AAm} + m_{AAc} + m_{BIS})$ was varied between 0.3 and 2.3 % (Supplementary Fig. 2). As expected, C_c affects the hydrogel swelling properties, leading to an inverse relation between C_c and particle size (Fig. 1d).

Coating MPs with ligands is critical for triggering specific cellular behavior and conjugation with fluorescent molecules is required for visualization of the particles and their deformation in microscopy applications. We incorporated acrylic acid into the gel mixture to allow straightforward and efficient covalent coupling of primary amine groups to the DAAM-particles using carbodiimide crosslinking chemistry[24]. DAAM-particles were functionalized with both fluorescently conjugated bovine serum albumin (FITC-BSA) and small fluorescent molecules (TRITC-Cadaverine (Cad)) (Fig. 1e). Confocal

imaging revealed highly homogeneous coupling of both protein and reactive dye to the microporous DAAM-particles.

The ideal force-reporting microparticle has a homogeneous and isotropic network structure, which underlies equally homogeneous elastic properties. However, initiating polymerization at the droplet boundaries, or subsequent gel swelling, could potentially lead to a radially inhomogeneous network structure. Derivatization of the particles could also affect particle mechanical properties and lead to further inhomogeneities. Therefore, we evaluated the radial fluorescent intensity profile (n > 100 particles) of both FITC-BSA and TRITC-Cad conjugated to DAAM-particles. (Fig. 1f, Supplementary Fig. 2) Simulation of the fluorescent signal of a perfectly homogeneous sphere, by convolution with an experimentally determined point spread function (PSF) (Supplementary Fig. 3), accurately reproduced the experimental radial intensity profile, independent of crosslinker density (Fig. 1f, Supplementary Fig. 2). The lack of radial deviations from a homogeneous sphere, combined with the homogeneous appearance of individual particles, strongly suggests that these particles have uniform and isotropic polymer networks.

In addition to intraparticle homogeneity, strong interparticle uniformity is critical for application of microparticles as force sensors. To evaluate particle-to-particle variation, we measured quantitative 3D refractive index (*RI*) maps of individual DAAM-particles (Fig. 1g). These measurements revealed *RI* values of 1.3349 ± 0.0001 (standard deviation (s.d.), n = 8) to 1.3381 ± 0.0001 (s.d., n = 29) for particles with C_c = 0.32% and C_c = 2.3%, respectively (Fig. 1g). The coefficient of variation (CV: calculated as the standard deviation divided by the relative *RI* difference between particle and medium) within each condition were markedly low at 0.03 – 0.1. Moreover, the similarity of the standard deviations between samples suggests that the observed variation may be dominated by the measurement error, and the particle-to-particle variation in polymer network density is potentially even lower.

The close match of *RI* between these particles (1.3349 – 1.3381) and the medium (RI_{PBS} = 1.334) also represents a significant benefit over glass (RI_{GLASS} = 1.45) or polystyrene (PS, RI_{PS} = 1.59) beads for many microscopy applications, including their use as target models for phagocytosis. The optical distortions, *i.e.* the reflection and

refraction of light, caused by a particle depends on $RI_{medium} - RI_{MP}$. For DAAM-particles this value is 0.001 - 0.005, whereas for glass or polystyrene these values are typically 100-fold higher (Fig. 1h). We compared confocal images of DAAM and PS particles with volumetric and surface labels (Fig. 1i). Z-slices of both particles revealed apparently equivalent signals. Axial slices of the volume of PS-particles, however, showed a distorted shape (the upper hemisphere appears axially elongated by $\sim RI_{medium}/RI_{MP}$) and an inhomogeneous signal. Furthermore, the fluorescent signal from the upper hemisphere's surface is reflected off the PS-particle surface and is largely not captured on the camera. Such lensing effects are barely noticeable for DAAM-particles. Finally, due to the porous nature of DAAM-particles, the advantageous optical properties are rather independent of the medium, as evidenced from repeating these measurements in vectashield with *RI* 1.45 (Fig. 1h, Supplementary Fig. 4).

To allow quantitative force sensing with deformable DAAM-particles, we characterized their mechanical properties by atomic force microscopy (AFM). We used pyramidal tips with a large end radius (~600 nm), which allow imaging of spherical particles, and indentations in the Hertzian regime because of the large end radius (Fig. 1j). Imaging of single particles before indentation allows precise localization of the centroid of the particle for subsequent indentations (Fig. 1j). Moreover, it provides an estimate of the particle shape, revealing that DAAM-particles are significantly deformed due to surface adhesion, forming spherical caps with contact radius > 4 um (Supplementary Fig. 5). This renders the indentation-induced deformation of the bottom of the DAAM-particles, which is in contact with the surface, negligible compared to the deformation of the upper part, which is in contact with the AFM tip. Nano-indentations at the particle's centroids showed typical Hertzian force responses and revealed cell-like rigidities, as quantified by the Young's moduli (E_y) between 0.3 and 3.9 kPa, for C_c = 0.32 – 2.3 % (Fig. 1k). For the more rigid particles, we found up to 1.5-fold higher moduli after conjugation of the particles with BSA. Importantly, the Young's moduli are 5-10 fold lower than bulk hydrogels of similar composition (Supplementary Fig. 5). Such discrepancy may be caused by the differences in polymerization conditions (*e.g.* different initiator and temperature) or gel swelling, and illustrate the importance of direct mechanical characterization of MPs.

Superresolved shape analysis of DAAM-particles

To determine the accuracy with which the particle shape can be reconstructed and to generate a reference shape measurement of undeformed particles, we imaged adherent particles in Vectashield mounting medium (*RI* ~1.45). The 3D shape of individual particles was reconstructed by processing confocal imaging stacks, encompassing deconvolution, and edge detection and localization steps (Supplementary Fig. 6). We varied the laser power to obtain particle images with various signal-to-noise ratios (SNR) (Fig. 2a) and estimated our localization precision as the local surface roughness R_{rms} observed over a small area (1 μm^2). Only the DAAM-particles' upper hemispheres were analyzed to exclude effects of deformation due to adhesion to the glass substrate. Due to the non-isotropic resolution in confocal microscopy, the local R_{rms} depended on the position on the particle. Therefore, we separately quantified the R_{rms} at the equator (latitude < 15°) and at the particle apex (latitude > 75°), which are dominated by the resolution in z and xy respectively (Fig. 2b). Even at modest SNR (~15) the localization precision in z (~200 nm) and xy (~40 nm) exceeded the nominal resolution (full width at half maximum of the PSF) in the corresponding direction. The principle enabling us to superresolve the particle boundary is similar to single molecule localization techniques[25,26] (Supplementary Discussion). With increasing SNR (>100), the localization further improved (z: ~40 nm, xy ~20 nm), also leading to a 2.5-fold reduction in the resolution anisotropy (Fig. 2b).

Aside from edge localization precision, the accuracy with which deformations can be measured (and forces recovered) also depends on the particle shape in the absence of externally applied forces. Deviations from a perfect spherical shape can, for example, be caused by deformation of the emulsion droplets during gelation. In addition, apparent shape deviations can arise from imaging artifacts like drift during recording of confocal stacks. To measure such deviations we quantified 1) the global R_{rms}, calculated over the entire upper particle hemisphere and 2) the sphericity, defined as the surface area of a sphere with equal volume to the particle divided by the observed particle surface area (1 for a perfect sphere). Global R_{rms} measurements revealed small (50 ± 25 nm) overall surface roughness, corresponding to deviations of less than 1% of the particle radius (Fig. 2c). Sphericity calculations corroborated that DAAM-particles are very spherical

(ψ = 0.9988 ± 0.0004). Finally, we decomposed the DAAM-particle shape using spherical harmonics for spectral analysis (Supplementary Note 1), which revealed that deviations from a perfect sphere have no characteristic length scale (white noise) (Fig. 2d).

Macrophage-like cells induce localized target deformations during phagocytosis

Cellular forces have an important role during target engulfment in phagocytosis. Such phagocytic forces have previously only been measured in the frustrated state on flat substrates[27], and our conjugatable and deformable DAAM-particles present an ideal tool for measuring them on particles with more physiological curvature. We exposed J774 murine macrophage-like cells to soft DAAM-particles (0.3 kPa, C_c = 0.32%) that were labeled with TRITC-Cad and functionalized with BSA and anti-BSA immunoglobulin G (IgG). J774s showed strongly ligand-dependent attachment to, and internalization of, antibody-coated DAAM-particles (Supplementary Fig. 7). After fixation of the cells, a secondary antibody was added, which is sterically unable to diffuse into the cell-target contact area[28]. Because the secondary antibody only binds the exposed DAAM-particle surface, it provides a measurement of the degree to which the phagocytic process has progressed (Fig. 3). Confocal images of DAAM-particles undergoing phagocytosis revealed local cell-induced deformations at all stages of the process.

To comprehend the full extent of phagocytic target deformation by macrophage-like J774s, the 3D shape of particles in various stages of phagocytic engulfment was reconstructed (Supplementary Fig. 6, Fig. 4). In addition, determination of the fluorescent intensity of the secondary antibody over the particle surface allowed determination of the contact area between the phagocyte and the DAAM-particle, and the location of the base of the phagocytic cup (Supplementary Fig. 6, Fig. 4). This analysis revealed complex and distinct patterns of deformation, suggesting an intricate series of mechanical interactions throughout phagocytosis.

Reference-free estimation of normal and shear stresses from particle shape

To reveal the cellular forces exerted on phagocytic targets, we calculated the traction forces from the observed particle shapes. In classical TFM, the displacement

field is measured directly, while in our method, the 3D shape of DAAM-particles is measured with high resolution instead. The surface displacement field is not uniquely determined by the surface shape, since multiple displacement fields can lead to the same shape. To derive traction forces, we thus solved the inverse problem of inferring the traction forces given the observed particle shapes and the traction-free regions from the fluorescent immunostaining (Supplementary Fig. 6). This is accomplished by an iterative optimization procedure described below (Fig. 5a).

We start with a trial surface displacement field $\boldsymbol{u}(\theta, \varphi)$, where θ, φ are co-latitude and longitude respectively, from which we can rapidly obtain the full elasticity solution, including the stress field everywhere in the particle, the traction force $\boldsymbol{T}(\theta, \varphi)$ on the surface, and the elastic energy E_{el} using the spherical harmonics-based method[19]. Given the surface displacement field, we also can compute the corresponding shape as described by a radial function $r(\theta, \varphi)$. The difference between the trial shape $r(\theta,\varphi)$, and the measured shape $r_0(\theta, \varphi)$ is quantified by function $D(r; r_0)$, and the residual tractions on the regions supposed to be traction-free is quantified by function $R(\boldsymbol{T}; \partial\,\Omega_t)$ (see Methods). A cost function f is then constructed for the trial solution $\boldsymbol{u}$:

$$f(\boldsymbol{u}) = D^2(r; r_0) + \alpha R^2(\boldsymbol{T}; \partial\,\Omega_t) + \beta E_{\mathrm{el}},$$

where α and β are weighing coefficients. The cost function is iteratively minimized using the conjugate-gradient algorithm for different choices of α and β. The elastic energy is included in the cost function to penalize unphysical solutions that produce the same surface shape. The final choices of the weighing coefficients are determined based on the dependence of converged solutions on α and β (Supplementary Fig. 8). The final solution is able to reach shape difference below the noise level (< 50 nm), and small residual tractions (<10 Pa) on the traction-free region (Fig. 5).

The minimization of the cost function requires the solution of the elasticity problem for millions of trial displacement fields $\boldsymbol{u}(\theta, \varphi)$. Therefore, each elasticity problem needs to be solved very fast. Using the spherical harmonics-based method, we can solve each elasticity problem within 0.007 second, so that the cost function can be minimized within a day (Methods). This would not have been possible if the elasticity problem were solved using general-purpose elasticity solvers such as the finite element method (FEM).

High resolution and 3D analysis of phagocytic forces and target deformation

The method presented here allows studying cellular forces throughout phagocytosis and resulting target deformation in great detail. Observations in the initial stage of phagocytosis (particle 1, 9% engulfed) provided evidence of the cell compressing its target in discrete spots (Fig. 4a, Supplementary Video 1). Computation of the mean curvature H over the particle surface clearly showed that the deformation induced by the cell consists of three distinct spots of approximately 1 μm in diameter. The compressive stresses causing this deformation were ~50 Pa (Fig. 5b). Approximately 9% of the DAAM-particle was covered by the cell and the compressive forces were located centrally in this area (Fig. 5b).

Significantly larger target deformations of up to 1 μm in the radial direction were observed during the stage of pseudopod extension (particle 2, 34% engulfed) (Fig. 4b, Supplementary Video 2). The majority of compressive deformation by the cell was localized in a ring, and was accompanied by a ~6% elongation in the direction normal to the ring. The peak of the inward deformations coincided closely with the extension of the pseudopod as estimated from the exposed surface labeling, while the indentation induced within the ring is markedly heterogeneous with clear dents and bumps (R_{rms} = 120 nm) (Fig. 4b, Supplementary Fig. 9). This heterogeneity appears to be caused by equally varied exertion of normal stresses from 20 to 100 Pa (Fig. 5b). Shear stresses up to 50 Pa were also concentrated in the ring (Fig. 5c). Perhaps surprisingly, the cell also appeared to pull from the cup base with tensile stresses having similar magnitude to the compressive stresses. The entire engulfed surface exposed greater heterogeneity in curvature than the particle surface not in contact with the cell (Fig. 4b). In particular, two distinct pits were visible close to the base of the phagocytic cup (indentation depths: ~250 and ~700 nm). Such deformations were caused by localized compressive stresses up to 100 Pa, and were not expected since in this phase of phagocytosis the cytoskeletal actin is being cleared from the cup base[29].

Observations in the stage of cup closure (particle 3, 84% engulfed) indicated compression by the cell in a rather smooth ring, and an approximately 7% particle elongation normal to the ring (Fig. 4c, Supplementary Video 3). Although deformations

in the ring were less strong than observed in particle 2, the underlying normal stresses were mostly higher (50 – 100 Pa), which can be explained by compression of the target throughout the cell-target contact area (Fig. 5b). The smaller variation in force also resulted in a more homogeneous appearance of the ring (R_{rms} = 60 nm) than in particle 2 (Fig. 4c, Supplementary Fig. 9). Interestingly, the peak of the inward deformation and force was not localized at the cell boundary but trailing approximately ~1 μm behind. Curvature and traction patterns were visible throughout the phagocytic cup, and seemed somewhat concentrated at the phagocytic cup base with 2 notable dents (~90 Pa). Such pits, which were also visible in particle 2, resemble the size and shape of podosomes[30,31], and could indicate a role for these mechanosensitive structures in phagocytosis.

Finally, a fully internalized particle (particle 4), which lacked fluorescent secondary immunostaining (Fig. 4d, Supplementary Video 4), was subjected to some of the strongest indentations (~ 1 μm, ~600 Pa) by the cell. These strong normal stresses were also accompanied by large shear stresses up to 100 Pa (Fig. 5c). The deformations consisted of multiple (at least 8) dents, ranging between 1-2 μm in diameter. The brightfield image (Fig. 3) was used to estimate the location of the cup base, revealing that these compressive deformations arise from the site of phagocytic cup closure. Perhaps this indicates that actin that accumulates during cup closure[32] contributes to the repositioning of the maturing phagosome towards the center of the cell.

DISCUSSION

Here we have introduced batch-produced, deformable, and readily derivatizable microparticles as cellular stress sensors, as well as a novel numerical method to calculate forces exerted on them by cells. Aside from force-sensing applications, such particles can offer several key advantages as model targets for studying cellular processes, such as phagocytosis and immunological synapse formation. They allow the unique possibility to mimic the size, rigidity, and relevant chemical characteristics of cells. The tunability of the particles' Young's moduli between 0.3 and 10 kPa covers a significant part of the range exhibited by various celltypes[33], and can likely be expanded further. In contrast, polystyrene or silica, which are often used as model targets, have Young's moduli of 2 GPa and 70 GPa, respectively. This is 10^5 - 10^7 fold larger than cells, and most other biological materials. Moreover, for microscopy applications, the small refractive index difference between DAAM-particles and the surrounding medium ensures little optical distortion in imaging of particles themselves, and will also result in improved visualization of surrounding (cellular) structures.

Two recent reports have described similar deformable hydrogel particles consisting of AAm or alginate that can be used as passive force sensors in multicellular aggregates and tissues[15,16]. Compared to the single microfluidic channel methods chosen previously, our batch particle synthesis method is simpler, and requires little specialized expertise or facilities. In terms of resulting particle properties, our production method leads to monodispersity (CV $\lesssim$ 0.1) approaching that reached with a single microfluidic channel (CV ~ 0.05). Importantly, our observed particle-to-particle variation in optical and mechanical properties is markedly low. For MPs with refractive index ~1.4, previously a spread on the order of 0.001 was reported[16], while we observe a significantly lower spread of ~0.0001. Our particles also appear mechanically homogeneous, with CVs in Young's moduli between 0.08 - 0.30 for stiff to soft particles. Such particle uniformity may be related to our choice for an oil-soluble polymerizing agent (Supplementary Discussion). We also do not observe any increase in variation of particle material properties after functionalization, presumably because of the efficient and homogeneous conjugation to the acrylic acid incorporated in DAAM-particles. Such efficient

conjugation is also crucial for robust triggering of specific cellular responses and, by allowing homogeneous staining, particle edge localization.

Currently, the dominant strategy in traction force microscopy is (random) embedding of fluorescent tracer particles in hydrogels, which, when compared to a reference state, allow measurement of the displacement field and relatively straightforward calculation of the stress field. Recently, this approach was extended to deformable microparticles (~25 μm) by Mohagheghian *et al.*[15]. Our contrasting approach, which focuses on accurate measurement of the particle boundary, has several key benefits: 1) The magnitude of deformation within elastic materials typically scales with $1/l$, where l is the distance to the site of application of the stress. Thus, measuring stresses directly at the particle boundary enhances the sensitivity to small forces. Indeed, we are able to resolve small tractions (~10 Pa). 2) For evaluation of traction forces, the stress field in the elastic gel is multiplied with its surface normals. Without precise knowledge of the location of the surface, certain assumptions need to be made. For microparticles, it was previously assumed that the deformed shape was convex[10]. However, throughout phagocytic engulfment we observed many concave surface regions (*i.e.* areas with mean curvature $H < 0$, Fig. 4), which are hence critical for a complete description of exerted forces by the cell. 3) In contrast to embedding randomly distributed tracer particles, our method provides a reference-free estimate of cellular stresses. This simplifies experimental procedures, is less disruptive to the sample, and will allow larger throughput studies. Finally, our approach is best adapted for relatively small particles (~10 μm), where the advantages mentioned above become increasingly important, since relatively more information is contained near the surface.

We have focused on phagocytosis and have illustrated the mechanical complexity of this process. However, as also exemplified by the development of a similar approach for quantifying forces during development in zebrafish embryos by Träber *et al*[34], the method presented here is broadly applicable in the study of inter- and intracellular forces *in vitro* and *in vivo*.

METHODS

Synthesis of deformable acrylamide acrylic-acid microparticles

All reagents were reagent grade and purchased from major chemical suppliers unless otherwise specified. All acrylamide mixtures contained 150 mM NaOH, 0.3% (v/v) tetramethylethylenediamine (TEMED), 150 mM MOPS in addition to the acrylamide (AAm), acrylic acid (AAc) and crosslinker N,N'-methylenebisacrylamide (BIS) with a final pH of 7.4. The total mass concentration of acrylic components ($C_T = C_{AAm} + C_{AAc} + C_{BIS}$) was 100 mg/mL, and the relative concentration of acrylic acid ($m_{AAc}/(m_{AAm} + m_{AAc} + m_{BIS})$) was 10% for all mixtures. The crosslinker concentration ($C_c = m_{BIS}/(m_{AAm} + m_{AAc} + m_{BIS})$) was varied between 0.32% and 2.3%, as indicated throughout the text and figures. Prior to extrusion, the mixture was degassed for 15 minutes and stored under nitrogen until the extrusion process was complete. Tubular hydrophobic Shirasu porous glass (SPG) membranes of 20 mm length, 10 mm outer diameter and with pore size (diameter) 0.5 – 3 μm, (SPG Technology Co.) were sonicated under vacuum in HPLC grade n-heptane to remove gas trapped in the membrane. The membrane was mounted on an internal pressure micro kit extruder (SPG Technology Co.) and immersed into an oil phase (~125 mL) consisting of hexanes (99% ACS reagent, mixed isomers) and 3% (v/v) Span 80 (Fluka, 85548). 10 mL of gel mixture was extruded through SPG membranes under nitrogen pressure of approximately 7 kPa, 8 kPa, 30 kPa and 100 kPa, for membranes with pore size 3 μm, 1.9 μm, 1.1 μm and 0.5 μm, respectively. The oil phase was continuously stirred at 300 rpm and kept under nitrogen atmosphere in a 3-neck water-jacketed flask (Fig. 1a, custom made by Chemglass Life Sciences), during extrusion (and polymerization). After completion of extrusion, the emulsion temperature was increased to 60 °C. Once the temperature equilibrated, DAAM-particle polymerization was induced by addition of ~225 mg 2,2'-Azobisisobutyronitrile (AIBN) (1.5 mg/mL final concentration). The polymerization reaction was continued for 3h at to 60 °C and then at 40 °C overnight. Polymerized particles were subsequently washed (5x in hexanes, 1x in ethanol), dried under nitrogen flow for approximately 30 minutes, and resuspended in PBS (137 NaCl, 2.7 mM KCl, 8.0 mM Na_2HPO_4, 1.47 mM KH_2PO_4, pH 7.4).

Microparticle functionalization

DAAM-particles were diluted to 5% (v/v) concentration and washed twice in activation buffer (100 mM MES, 200 mM NaCl, pH 6.0). They were then incubated for 15 minutes in activation buffer supplemented with 40 mg/mL 1-ethyl-3-(3-dimethylaminopropyl)carbodiimide, 20 mg/mL N-hydroxysuccinimide (NHS) and 0.1% (v/v) Tween 20. Afterwards they were spun down (2 min, 16000 g) and washed 4x by centrifugation in PBS8 (PBS adjusted to pH 8.0 with NaOH) with 0.1% Tween 20. Immediately after the final wash the particles were resuspended in PBS8 with BSA (Sigma, A3059) (or FITC-BSA for the experiment in figure 1e & supplementary figure 2) (for concentrations see Supplementary Table 1). After 1h the cadaverine-conjugate was added: either Alexa Fluor 488 Cadaverine for the figures illustrating the lensing effect (Fig. 1i, Supplementary Figure 4) or Tetramethylrhodamine Cadaverine for all other experiments (Supplementary Table 1). After 0.5h unreacted NHS groups were blocked with a solution of: 100 mM TRIS and 100 mM ethanolamine (pH 9). Finally, DAAM-particles were spun down (30 s, 8000 g) and washed 4x in PBS. DAAM-particles were further functionalized with anti-BSA rabbit IgG (MP Biomedicals, 0865111) in PBS (for concentrations see Supplementary Table 1) and spun down (30 s, 8000 g) and washed 3x with PBS for phagocytic assays and lensing effect experiments. For the lensing effect experiments, DAAM-particles were resuspended in 4.5 μg/ml Alexa Fluor 546 goat anti-rabbit IgG in PBS, again followed by 3 spins and washes (PBS). 10 μm yellow-green fluorescent carboxylate modified polystyrene beads (Polysciences) were functionalized with BSA, anti-BSA rabbit IgG, and Alexa Fluor 546 goat anti-rabbit IgG in similar fashion (Supplementary Table 1).

Fluorescent conjugation of BSA

Fluorescein isothiocyanate conjugated BSA (FITC-BSA) was made according to previously published techniques[35]. Briefly, 800 μl of 5 mg/ml FITC in DMSO was added to 100mg of BSA in 10 mL of carbonate buffer (pH 9.0). After 30 minutes of stirring at room temperature the reaction was continued at 4 °C overnight. The following day the labeling reaction was quenched with 1 mL of 1 M Tris HCL (pH 8.8) followed by dialysis against PBS for 2 hours at 4 °C. The dialysate was concentrated to 1.5 mL by

placing the dialysis bag in solid sucrose, and desalted over a G25 column equilibrated with PBS.

Microparticle size measurements

For microparticle size measurements, particles were imaged with a 20x NA 0.4 objective using phase-contrast. For the smallest particles, which were extruded through 0.5 μm pore size SPG filters, a 40x NA 1.3 objective was used for imaging. Images were analyzed in ImageJ, by smoothing (2x), performing edge detection, binarizing images by thresholding and filling holes. Finally, adjacent particles were separated using the watershed algorithm, and particle radii were estimated from particle areas.

Microparticle refractive index measurements

3D quantitative refractive index (*RI*) maps were measured on a 3D Cell Explorer (NanoLive) and analyzed using ImageJ. Z-slices of the 3D tomogram through the center of individual DAAM-particles were selected for analysis. Histograms of the *RI* in a small region of interest around the DAAM-particle revealed a clear bimodal distribution. $RI_{MP} - RI_{medium}$ was then measured as the distance between the two peaks of the *RI* histogram. RI_{medium} was measured for PBS (1.334), or used as specified by the manufacturer as 1.45 for vectashield mounting medium (Vectorlabs, H-1000).

Atomic force microscopy measurements

Unfunctionalized DAAM-particles and BSA + Cad- DAAM-particles were attached to poly-L-lysine coated and untreated circular 25-mm glass coverslips, respectively. All coverslips were cleaned for 5 minutes in boiling water with detergent Micro-90, rinsed with milliQ water and dried at 200 °C. For poly-L-lysine coating, coverslips were then incubated in a 0.1 mg/mL poly-L-lysine (Sigma, P8920) solution for 1 h, rinsed with water and left to dry at room temperature. A 50 μl drop of DAAM-particle suspension (~2% solids (v/v)) in PBS was added to the coverslips and subsequently washed 3 times with PBS. AFM experiments were performed with large radius (~600 nm) pyramidal tips (LRCH-15-750-R, Nanoscience Instruments) on a Bruker Bioscope Resolve setup. The spring constant of individual cantilevers (~ 0.13 N/m) was calibrated by thermal tuning.

Before indentation, particles were imaged in peak force tapping mode (peak force setpoint 0.5 – 1 nN). Subsequently, 2-5 nanoindentations were performed on the center of particles. AFM data was analyzed using custom Matlab software. DAAM-particle shape was determined as described previously for small vesicles.[36] Briefly, a spherical arc was fit to upper part of the DAAM-particle (exceeding half its height) to obtain the radius of curvature R_{MP}, which was corrected for tip convolution by subtracting the tip radius (R_{tip}). Assuming that adherent particles form spherical caps, the shape was then approximated from R_{MP} and the particle height (Supplementary Fig. 5). Indentation curves (or force deformation curves, FDCs) were first processed by correction for drift in the baseline and subtraction of a fit to the cantilever response, which was obtained by performing indentations on bare glass surfaces. The resulting DAAM-particle indentation curves were analyzed by fitting a Hertzian model up to 0.5 R_{tip}, with the contact point as a fitting parameter. For these fits, the effective radius R^*, where ($1/R^* = 1/R_{tip} + 1/R_{MP}$), was used. FDCs for the stiffer DAAM-particles (C_c = 0.65 % and C_c = 2.3 %) were analyzed above 50 pN force. Due to the low rigidity of the softest DAAM-particles (C_c = 0.32%) a force threshold of 10 pN was used. The Young's moduli (E_y) obtained from each of the 2-5 FDCs for individual particle were averaged to reduce the measurement error of the DAAM-particles. For the Young's moduli calculations, DAAM-particles were assumed to be incompressible (Poisson ratio = 0.5), which was previously shown to be a good approximation for bulk[37] and microparticle[16] acrylamide gels. For bulk gel measurements, hydrogels, covalently bound to glass substrates, were prepared as described under "PSF measurements", but with compositions, and buffer conditions, identical to the DAAM-particles (for all three crosslinker concentrations). Measurements were performed with spherical tips (SiO_2) with ~300 nm radius (NovaScan Technologies). Indentation curves were analyzed as described for the DAAM-particles.

Cell culture

Murine macrophage-like cells J774A.1 (ATCC, TIB-67) were maintained and subcultured according to the methods recommended by ATCC. Briefly, cells were maintained in DMEM medium (Gibco, 11965-092) supplemented with 10% FBS

(GemBio, 900-108), and antibiotics and antimiotics (Gibco, 15240-062). Subcultures were prepared by scraping.

Phagocytic assays

For phagocytic assays, cells were transferred to 12-well glass bottom plates (Cellvis, P12-1.5H-N) ($1.5x10^5$ cells/well). 1h before addition of DAAM-particles, the medium was replaced by L-15 medium without serum. 15 minutes before addition of the DAAM-particles Hoechst 33258 (ThermoFisher, H3569) was added for a final concentration of 1 μg/mL in each well. The medium was then replaced with 200 μL L-15 per well including the DAAM-particles ($7.5x10^5$ DAAM-particles/well), the plate was spun for 1 min. at 300 g and incubated at 37 °C. Cells where fixed by direct addition of 1 ml of 4% formaldehyde (J.T. Baker, 2106-01) in PBS after 5 min for the phagocytic deformation assay (Fig. 3-5) and after 30 min for the uptake efficiency assay (Supplementary Fig. 7). Cells were rinsed vigorously by pipetting up and down with PBS to remove particles not in contact with cells. Exposed surface of the particles was immunostained with 4 μg/mL Alexa Fluor 647 donkey anti-rabbit IgG (ThermoFisher Sci., A31573) in PBS. After 30 minutes the wells were rinsed with PBS (3x) and imaged on a confocal microscope.

Confocal Microscopy

3D confocal imaging was performed using a spinning disk CSU-W1 scanner unit (Yokogawa) and a DMi6 inverted microscope, equipped with a 100x (NA 1.40) objective (Leica Microsystems). Excitation was done with solid state lasers (100 mW 488 nm, 50 mW 560 nm, 100 mW 642 nm) and images were captured on an Ixon Ultra EMCCD camera (Andor). Z-stacks with 100 nm step size were recorded using a piezo stage insert (LUDL Electronic Products, 96A900). The setup was operated using MicroManager[38].

Microparticle 3D shape reconstruction

Image analysis was performed with custom software in Matlab. Individual microparticles were segmented based on intensity thresholding confocal z-stacks, using the dip in the distribution of the logarithm of voxel intensities as the threshold. The centroid of DAAM-particles was estimated, and they were isolated in ~20 × 20 × 30 μm regions of interest

(ROIs) that were used for further processing. First, images were deconvolved with a point spread function (PSF), measured ~8 μm from the sample surface (Supplementary Fig. 3). Deconvolution was performed with 25 iteration steps using a Landweber algorithm, and was implemented using DecovolutionLab 2[39]. Background subtraction was performed by averaging the Z-slices outside the ROI along the axial direction and subtraction of the resulting 2D image from each slice of the ROI. At this point, cubic interpolation along the z-axis was used to equalize the voxel dimensions. Edge detection was performed using the 3D Sobel operator[40] (Supplementary Fig. 6), after which the total edge magnitude was calculated as the root mean squared of the three resulting images. For superlocalization of edge coordinates, first a volume estimate of each DAAM-particle was made, based on the number of thresholded voxels, which was converted into a particle surface area estimate assuming a perfect sphere. The number of edge coordinates N was determined as the particle surface area divided by the area of a circle with radius 250 nm (for the DAAM-particles subjected to phagocytosis) or 500 nm (for undeformed spheres, in which case we wanted to prevent correlation between neighbouring points). Longitude φ and co-latitude θ for approximately equally spaced points were found as:

$$\varphi = n\pi\left(3 - \sqrt{5}\right) \bmod 2\pi$$

$$\theta = \arccos\left(1 - \frac{2n}{N-1}\right)$$

where n = 0,1,….,N-1. Modulus 2π is taken, such that $\varphi \in [0, 2\pi)$.

Cubic interpolation was used to estimate the intensity values along lines originating from the particle centroid in the directions of the angles determined above. Then a Gaussian function was fit to each line profile to determine the location of the edge with subpixel precision.

Smoothing of edge coordinates

Edge coordinates were smoothed (for sphericity, curvature and force calculations) using an equivalent of a 2D moving average, operating on the radial component of edge coordinates. Great circle distances between edge coordinates with indexes i and j were calculated along a perfect sphere:

$$d = \arccos\left(\sin\theta_i \sin\theta_j + \cos\theta_i \cos\theta_j \cos\left(\varphi_i - \varphi_j\right)\right) R,$$

where R is the equivalent diameter of a sphere to the particle. The radial component of the edge coordinates was then averaged within the given window size (1 μm^2).

Calculation of particle and surface properties

First a triangulation was generated between points with the same angles (longitude and latitude) as the particle edge coordinates, but on a unit sphere. This allows using a convex hull approach to connect all data points and not leave any gaps. The particle surface area (S) was then calculated as the sum of the surface areas of all triangles. The particle volume (V) was calculated as the sum of the (signed) volumes of tetrahedra, which were formed by connecting all triangles with an arbitrary point. The particle centroid was determined as the volume-weighted sum of the tetrahedra centroids. Before calculation of sphericity and surface curvature, the radial component of edge coordinates was first smoothed within a 1 μm^2 window (see above). This was done because of the high sensitivity of these measures to high frequency noise. Sphericity was calculated as $\Psi = (\Psi^{1/3}*6*V^{2/3}/S)/2^{1/3}$, where the division by $2^{1/3}$ was used when only the upper hemisphere was analyzed, as it is a correction that guarantees that Ψ cannot exceed 1 for non-closed shapes. For surface curvature calculations, first principal curvatures (k_1 and k_2) of the triangulated mesh were determined as described previously[41]. Finally, mean curvature $H = (k_1 + k_2)/2$ and Gaussian curvature $K = k_1k_2$ were calculated. Local root-mean-squared surface roughness (R_{rms}) measurements were performed by using great circle distances to find points within a 1 μm^2 area (as above, typically 6-8 points), and then taking the standard deviation of the radial component of these points. Global R_{rms} was calculated similarly, but over the entire upper hemisphere.

Stress-free boundary analysis

Analysis of the immunostaining of the free particle surface was performed in custom Matlab software (Supplementary Fig. 6). First, images were deconvolved as described above. Then, cubic interpolation was used to estimate the intensity values along lines originating from the particle centroid (as determined during particle shape analysis). A regular grid in spherical coordinates (as opposed to an approximately equidistant grid used in particle shape analysis) was used, to simplify later image processing steps (in

particular the active contour algorithm described below). The number of points in the regular grid was approximately equal to the number of points used for shape analysis. After generating line profiles, the integrated intensity I_{tot} under the Gaussian was determined. I_{tot} was approximated as 1.065 * I_{max} * FWHM, where I_{max} is the maximum fluorescent intensity, FWHM is the full width at half maximum of the Gaussian peak in the intensity profile and 1.065 is the prefactor that appears during integration. I_{tot} appeared more uniform over the DAAM-particle surface than the I_{max}, because of the non-isotropic resolution in confocal microscopy. After generating a regular grid with total intensity values, this signal was binarized, initially by using a dip in the distribution of the logarithm of pixel intensities as the threshold. Then, a region-based active contour algorithm[42] ("snake") was used to optimize the mask. Finally, interpolation of the mask was used to determine for each particle edge coordinate if it was part of the freely exposed surface.

Reference-free estimation of both normal and shear stresses from particle shape

Force calculations were performed with custom Python software. The particle shapes were smoothed within a 1 μm^2 window, and the edge of the traction-free boundary was dilated and smoothed (Supplementary Note 2). Resolving traction forces from the particle shape can be defined as a linear elasticity problem on the sphere Ω with mixed boundary conditions: the surface shape expressed by the radial function $r_0(\theta, \varphi)$, and the region $\partial\Omega_t$ on which the traction $\boldsymbol{T}$ should be zero. The equilibrium condition of the elastic continuum Ω in terms of the displacement field $\boldsymbol{u}$ is:

$$\mu\nabla^2\boldsymbol{u} + \left(\frac{\mu}{1-2v}\right)\nabla(\nabla\cdot\boldsymbol{u}) = 0, (1)$$

where and μ is the shear modulus and v the Poisson's ratio. Given the displacement on the spherical surface, $\boldsymbol{u}(\theta, \varphi)$, the corresponding surface shape, *i.e.* the radial function $r(\theta, \varphi)$, can be constructed. Hence the mixed boundary condition can be written as $r(\theta, \varphi) = r_0(\theta, \varphi)$, and $\boldsymbol{T}|_{\partial\Omega_t} = 0$.

To solve this problem, we use an iterative approach which minimizes a cost function of trail surface displacement $\boldsymbol{u}(\theta, \varphi)$. For each trial $\boldsymbol{u}(\theta, \varphi)$, the elasticity equation is solved[19], and the corresponding stress fields, surface traction forces, and

elastic energy E_{el} are obtained. The trial surface displacement field is expanded into spherical harmonic space with a truncation of the degree number $l < l_{\max}$:

$$u_j(\theta, \varphi) = \sum_{l=0}^{l_{\max}} \sum_{m=-l}^{l} \hat{u}_{jlm}\, Y_l^m(\theta, \varphi)\,, (2)$$

where $\hat{u}_{jlm}$ are coefficients, and Y_l^m is the spherical harmonic function defined in Supplementary Note 3. In this work $l_{\max}$ = 20, which was chosen as a good balance between lateral spatial resolution (~800 nm) and computational time (~0.007s per traction evaluation). The traction is also expressed in the spherical harmonic space:

$$T_j(\theta, \varphi) = \sum_{l=0}^{l_{\max}} \sum_{m=-l}^{l} \hat{T}_{jlm}\, Y_l^m(\theta, \varphi)\,, (3)$$

where $\hat{T}_{jlm}$ are coefficients that are completely determined by $\hat{u}_{jlm}$.

Therefore, our goal is to determine the coefficients $\hat{u}_{jlm}$ that satisfy the mixed boundary conditions described above. Given that multiple displacement fields can give rise to the same surface shape, this problem does not have a unique solution. To infer the true traction forces, we solve the following minimization problem:

$$\min_{\{\hat{u}_{jlm}\}} f(\boldsymbol{u}) \;\; (4)$$

$$f(\boldsymbol{u}) = D^2(r; r_0) + \alpha R^2(\boldsymbol{T}; \partial\Omega_{\mathrm{t}}) + \beta E_{\mathrm{el}} \;(5),$$

where the cost function f has contributions from: (1) the shape difference $D(r; r_0)$; (2) a measure of residual traction magnitude on the traction-free region $R(\boldsymbol{T}; \partial\Omega_t)$; (3) and the elastic energy E_{el}. The elastic energy is included to select the most energetically favorable solution among the candidates that produce the same surface shape. Since D, R, E_{el} all have different units, the parameters α and β have the appropriate units to make f having the dimension of length squared. The selection of appropriate α and β values is discussed in Supplementary figure 8. For minimization of $f(\boldsymbol{u})$, we used the conjugate-gradient algorithm as implemented in SciPy. Convergence of the solution was reached after ~2000 iterations, while during each iteration traction forces were evaluated ~12000 times for gradient estimation.

The shape difference $D(r; r_0)$ is calculated as follows: We first generate a collection of sampling points using GLQ meshing (Supplementary Note 4) on the

undeformed spherical surface, whose spherical coordinates are $(r_i^s, \theta_i^s, \varphi_i^s), i = 1,2, \dots, n$, where n is the total number of points. Given the displacement field, we obtain the coordinates of these points after deformation $\left(r_i^d, \theta_i^d, \varphi_i^d\right)$. The deviation between the deformed surface shape from the measured shape $r_0(\theta, \varphi)$ is calculated as:

$$D(r; r_0) = \sqrt{\frac{1}{n}\sum_i \left\| \left[\left(r_i^d - r_0\left(\theta_i^d, \varphi_i^d\right)\right) \hat{\boldsymbol{r}}\left(\theta_i^d, \varphi_i^d\right) \cdot \boldsymbol{w}_n\right] w(\theta_i^s) \right\|^2}, (6)$$

where $\hat{\boldsymbol{r}}$ is the unit vector in radial direction, the weight function $\boldsymbol{w}_n$ and $w(\theta)$ are introduced to avoid the noise introduced by GLQ meshing and measuring (Supplementary Note 4); The residual traction magnitude on the traction-free region is calculated as:

$$R(\boldsymbol{T}; \partial\Omega_t) = \sqrt{\frac{1}{m} \sum_{(\theta_i^d, \varphi_i^d) \in \partial\Omega_t} \left\| [\boldsymbol{T}_i(\theta_i^s, \varphi_i^s) \cdot \boldsymbol{w}_n] \, w(\theta_i^s) \right\|^2}, (7)$$

where m is the total number of sampling points that is on the traction-free region.

Displacement solution based on spherical harmonics

As we are using an iterative method for solving the elasticity problem, it is essential to have fast computation of the shape $\boldsymbol{T}(\theta, \varphi)$ from the surface displacement field $\boldsymbol{u}(\theta, \varphi)$. The spherical harmonics method was previously developed as a fast solver for linear elasticity problems with spherical interfaces[19]. Briefly, the method can solve the stress field $\boldsymbol{\sigma}(r, \theta, \varphi)$ and the displacement field $\boldsymbol{u}(r, \theta, \varphi)$ everywhere in the elastic medium Ω, given the traction boundary condition $\boldsymbol{T}_{\mathrm{b}}(\theta, \varphi)$ or the displacement boundary condition $\boldsymbol{u}_{\mathrm{b}}(\theta, \varphi)$ on the spherical interface $\partial\Omega$. Using fast spherical harmonic transformation as provided by SHTools[43], the spherical harmonics method is more efficient and accurate than other general elasticity problem solvers such as finite-element methods (FEM)[19]. The implementation of the method is available online as ShElastic toolbox[19]. In particular, ShElastic toolbox pre-calculates a complete set of fundamental displacement solutions with $\boldsymbol{u}^{(K)}$ that satisfy the equilibrium equation (1):

$$\boldsymbol{u}^{(K)} = \frac{1}{2\mu}\left[-4(1-\nu)\boldsymbol{\psi}^{(K)} + \nabla\left(\boldsymbol{r} \cdot \boldsymbol{\psi}^{(K)}\right)\right], (8)$$

where the displacement potential vector $\boldsymbol{\psi}^{(K)}$ is defined in spherical coordinates as:

$$\boldsymbol{\psi}^{(K)} = \boldsymbol{\psi}^{(k,l,m)}(r,\theta,\varphi) = \hat{\boldsymbol{e}}_k\, r^l\, Y_l^m(\theta,\varphi), (9)$$

where $(K) = (k,l,m); (k = x,y,z; l = 0,1,2,\dots; m = 0,\pm 1,\dots,\pm l)$ indicates the 3-value index of the solution. The corresponding stress field $\boldsymbol{\sigma}^{(K)}(r,\theta,\varphi)$ in Ω, and the traction field $\boldsymbol{T}^{(K)}(\theta,\varphi)$ on $\partial\Omega$ are also pre-calculated. Then, the physical properties can be written as a linear combination of the fundamental solutions:

$$\boldsymbol{\sigma} = \sum_K a_K \boldsymbol{\sigma}^{(K)}, \qquad \boldsymbol{u} = \sum_K a_K \boldsymbol{u}^{(K)}, \qquad \boldsymbol{T} = \sum_K a_K \boldsymbol{T}^{(K)}, (10)$$

which are infinite series. In practice, we select a cutoff of $0 \le l \le l_{\max}$, and select all the m and k modes within the selected l modes to guarantee the symmetry of the deformation. The solution converges with exponentially decreasing error as $l_{\max}$ increases. The solution is searched on the solution space a_K as a vector.

Confocal voxel size calibration

Differences in axial (z) versus lateral (x,y) length measurements can arise from imperfect calibration of the microscope stage, and from refractive index mismatch between the sample and the immersion oil/cover glass. Hence, accurate calibration is necessary for proper reconstruction of the particle shape. First, confocal image stacks of 10 μm yellow-green fluorescent polystyrene beads (Polysciences, 18142) were recorded. Then, maximum intensity axial slices through individual particles were selected, and smoothed with a Gaussian filter (with a standard deviation of 3 pixels). Subsequently, edges of the homogeneously stained microspheres were detected using the 2D Sobel operator. The z-location of the equator, and the diameter of the particle, was determined by finding the horizontal line were the distance between the edges (at opposite sides of the particle) was maximal. Gaussian fits to the edge profiles were made to accurately determine the particle diameter. Next, the edge at the apex of the lower hemisphere of the particle (the "south pole") was localized using a similar approach. This difference in z-position of the equatorial plane with the south pole was used to estimate the apparent particle radius in z-direction. This approach, were only the lower hemisphere is used, prevents these measurements to be affected by the lensing effect caused by the particle (Fig. 1i, Supplementary Fig. 4). Finally, the ratio of the particle radius measured in xy and the

apparent particle radius in z was determined for multiple particles and average. In PBS, we found an axial elongation of 1.100 ± 0.003 (standard error of the mean (s.e.m.), n = 34). In vectashield (VS) we did not perform such a correction, since particles did not appear elongated in the axial direction (Fig. 2).

Point spread function measurements

For measurements of point spread functions (PSFs), red or yellow-green 100 nm fluorescent beads (ThermoFisher Sci., F8801/F8803) were embedded in flat adherent pAAm gels. Such hydrogels were prepared similarly to described previously[44,45]: clean 25 mm glass coverslips were incubated for 0.5h in 2 M sodium hydroxide. Coverslips were rinsed with distilled water and then incubated in 0.5% 3-Aminopropyltriethoxysilane (APTES) (Sigma, 919-30-2) in 95% ethanol. Coverslips were again rinsed with water and incubated in 0.05% glutaraldehyde for 1h, then rinsed with water and dried at 200°C. pAAm hydrogels consisting of acrylamide, and crosslinker N,N'-methylenebisacrylamide were made with C_T (C_{AAm} + C_{BIS}) 55 mg/mL, C_C (C_{BIS} / (C_{AAm} + C_{BIS})) 1.8 % (w/w) in distilled water. 2*10^{-5} % (v/v) 100 nm fluorescent beads and 0.8 % (v/v) TEMED were added to the mixture. 0.6 mg/mL ammonium persulfate (APS) (Fisher Sci., BP179) was added to initiate gel polymerization. A 3.6 μL drop of the mixture was added to a coverslip and was covered with a 12-mm untreated circular glass coverslip, which was gently pushed down. Polymerization was continued for 20 min at room temperature after which the small coverslip was removed. Gels were kept and imaged in PBS (pH 7.4) or in the mounting medium vectashield (Vector Laboratories, H-1000). Data was analyzed using custom Matlab software. Only beads that had no neighbours in a region of interest of 5 × 5 × 10 μm (x × y × z) around them were used for the analysis. After background subtraction, the total fluorescent signal of individual particles was normalized to 1. Particles were centered with subpixel resolution based on their weighted centroid (linear interpolation was used to approximate new pixel values). The position of the coverslip (z = 0) was determined based on background fluorescent signal, allowing us the measure the height of each particle with respect to the coverslip. Finally, the fluorescent signal of multiple particles (n > 50), with similar distances from the coverslip, was averaged.

References:

1. Vogel, V. & Sheetz, M. Local force and geometry sensing regulate cell functions. *Nat. Rev. Mol. Cell Biol.* **7,** 265–75 (2006).
2. Basu, R. & Huse, M. Mechanical Communication at the Immunological Synapse. *Trends Cell Biol.* **27,** 241–254 (2017).
3. Farhadifar, R., Röper, J. C., Aigouy, B., Eaton, S. & Jülicher, F. The Influence of Cell Mechanics, Cell-Cell Interactions, and Proliferation on Epithelial Packing. *Curr. Biol.* **17,** 2095–2104 (2007).
4. Leckband, D. E. & de Rooij, J. Cadherin Adhesion and Mechanotransduction. *Annu. Rev. Cell Dev. Biol.* **30,** 291–315 (2014).
5. Style, R. W. *et al.* Traction force microscopy in physics and biology. *Soft Matter* **10,** 4047 (2014).
6. Dembo, M. & Wang, Y.-L. Stresses at the Cell-to-Substrate Interface during Locomotion of Fibroblasts. *Biophys. J.* **76,** 2307–2316 (1999).
7. Polacheck, W. J. & Chen, C. S. Measuring cell-generated forces: A guide to the available tools. *Nat. Methods* **13,** 415–423 (2016).
8. Beningo, K. A. & Wang, Y. Fc-receptor-mediated phagocytosis is regulated by mechanical properties of the target. *J. Cell Sci.* **115,** 849–56 (2002).
9. Basu, R. *et al.* Cytotoxic T Cells Use Mechanical Force to Potentiate Target Cell Killing. *Cell* **165,** 100–110 (2016).
10. del Álamo, J. C. *et al.* Three-dimensional quantification of cellular traction forces and mechanosensing of thin substrata by fourier traction force microscopy. *PLoS One* **8,** e69850 (2013).
11. Legant, W. R. *et al.* Multidimensional traction force microscopy reveals out-of-plane rotational moments about focal adhesions. *Proc. Natl. Acad. Sci.* **110,** 881–886 (2013).
12. Franck, C., Maskarinec, S. A., Tirrell, D. A. & Ravichandran, G. Three-Dimensional Traction Force Microscopy: A New Tool for Quantifying Cell-Matrix Interactions. *PLoS One* **6,** e17833 (2011).
13. Campàs, O. *et al.* Quantifying cell-generated mechanical forces within living embryonic tissues. *Nat. Methods* **11,** 183–189 (2013).
14. Mongera, A. *et al.* A fluid-to-solid jamming transition underlies vertebrate body axis elongation. *Nature* (2018). doi:10.1038/s41586-018-0479-2
15. Mohagheghian, E. *et al.* Quantifying compressive forces between living cell layers and within tissues using elastic round microgels. *Nat. Commun.* 1–14 doi:10.1038/s41467-018-04245-1
16. Girardo, S. *et al.* Standardized microgel beads as elastic cell mechanical probes. *J. Mater. Chem. B* 1–43 (2018). doi:10.1039/C8TB01421C
17. Schwarz, U. S. & Soiné, J. R. D. Traction force microscopy on soft elastic substrates: A guide to recent computational advances. *Biochim. Biophys. Acta - Mol. Cell Res.* **1853,** 3095–3104 (2015).
18. Bergert, M. *et al.* Confocal reference free traction force microscopy. *Nat. Commun.* **7,** 12814 (2016).
19. Wang, Y., Zhang, X. & Cai, W. Spherical Harmonics Method for Computing the Image Stress Due to A Spherical Void. *arXiv* 1–29 (2018). doi:1806.11165
20. Vladisavljević, G. T. & Williams, R. A. Recent developments in manufacturing

emulsions and particulate products using membranes. *Adv. Colloid Interface Sci.* **113,** 1–20 (2005).
21. Nakashima, T., Shimizu, M. & Kukizaki, M. Membrane Emulsification by Microporous Glass. *Key Eng. Mater.* **61–62,** 513–516 (1992).
22. Nagashima, S., Ando, S., Makino, K., Tsukamoto, T. & Ohshima, H. Size Dependence of Polymer Composition in the Surface Layer of Poly(acrylamide-co-acrylic acid) Hydrogel Microspheres. *J. Colloid Interface Sci.* **197,** 377–382 (1998).
23. Omi, S., Katami, K., Yamamoto, A. & Iso, M. Synthesis of polymeric microspheres employing SPG emulsification technique. *J. Appl. Polym. Sci.* **51,** 1–11 (1994).
24. Liu, E. Y., Jung, S. & Yi, H. Improved Protein Conjugation with Uniform, Macroporous Poly(acrylamide- co -acrylic acid) Hydrogel Microspheres via EDC/NHS Chemistry. *Langmuir* **32,** 11043–11054 (2016).
25. Betzig, E. *et al.* Imaging Intracellular Fluorescent Proteins at Nanometer Resolution. *Science (80-.).* **313,** 1642–1645 (2006).
26. Rust, M. J., Bates, M. & Zhuang, X. Sub-diffraction-limit imaging by stochastic optical reconstruction microscopy (STORM). *Nat. Methods* **3,** 793–795 (2006).
27. Kovari, D. T. *et al.* Frustrated Phagocytic Spreading of J774A-1 Macrophages Ends in Myosin II-Dependent Contraction. *Biophys. J.* **111,** 2698–2710 (2016).
28. Wright, S. D. & Silverstein, S. C. Phagocytosing macrophages exclude proteins from the zones of contact with opsonized targets. *Nature* **309,** 359–361 (1984).
29. Marion, S. *et al.* The NF-κB Signaling Protein Bcl10 Regulates Actin Dynamics by Controlling AP1 and OCRL-Bearing Vesicles. *Dev. Cell* **23,** 954–967 (2012).
30. Labernadie, A. *et al.* Protrusion force microscopy reveals oscillatory force generation and mechanosensing activity of human macrophage podosomes. *Nat. Commun.* **5,** (2014).
31. Murphy, D. A. & Courtneidge, S. A. The 'ins' and 'outs' of podosomes and invadopodia: Characteristics, formation and function. *Nat. Rev. Mol. Cell Biol.* **12,** 413–426 (2011).
32. Swanson, J. a *et al.* A contractile activity that closes phagosomes in macrophages. *J. Cell Sci.* **112 (Pt 3,** 307–316 (1999).
33. Kuznetsova, T. G., Starodubtseva, M. N., Yegorenkov, N. I., Chizhik, S. a. & Zhdanov, R. I. Atomic force microscopy probing of cell elasticity. *Micron* **38,** 824–833 (2007).
34. Träber, N. *et al.* Polyacrylamide Bead Sensors for in vivo Quantification of Cell-Scale Stress in Zebrafish Development. *bioRxiv* (2018). doi:10.1101/420844
35. Greg T Hermanson. *Bioconjugate Techniques*. (2013).
36. Vorselen, D., MacKintosh, F. C., Roos, W. H. & Wuite, G. J. L. Competition between Bending and Internal Pressure Governs the Mechanics of Fluid Nanovesicles. *ACS Nano* **11,** 2628–2636 (2017).
37. Boudou, T., Ohayon, J., Picart, C. & Tracqui, P. An extended relationship for the characterization of Young's modulus and Poisson's ratio of tunable polyacrylamide gels. *Biorheology* **43,** 721–728 (2006).
38. Edelstein, A. D. *et al.* Advanced methods of microscope control using μManager software. *J. Biol. Methods* **1,** 10 (2014).

39. Sage, D. *et al.* DeconvolutionLab2: An open-source software for deconvolution microscopy. *Methods* **115,** 28–41 (2017).
40. Engel, K., Hadwiger, M., Kniss, J. M., Rezk-Salama, C. & Weiskopf, D. in *Real-Time Volume Graphics* 112–113 (A K Peters, Ltd., 2006).
41. Rusinkiewicz, S. Estimating curvatures and their derivatives on triangle meshes. in *Proceedings. 2nd International Symposium on 3D Data Processing, Visualization and Transmission, 2004. 3DPVT 2004.* 486–493 (IEEE, 2004). doi:10.1109/TDPVT.2004.1335277
42. Lankton, S. & Tannenbaum, A. Localizing region-based active contours. *IEEE Trans. image Process.* **17,** 2029–2039 (2008).
43. Wieczorek, M. A. & Meschede, M. SHTools: Tools for Working with Spherical Harmonics. *Geochemistry, Geophys. Geosystems* 1–19 (2018). doi:10.1029/2018GC007529
44. Yeung, T. *et al.* Effects of substrate stiffness on cell morphology, cytoskeletal structure, and adhesion. *Cell Motil. Cytoskeleton* **60,** 24–34 (2005).
45. Bastounis, E. E., Yeh, Y. & Theriot, J. A. Matrix stiffness modulates infection of endothelial cells by Listeria monocytogenes via expression of cell surface vimentin. *Mol. Biol. Cell* mbc.E18-04-0228 (2018). doi:10.1091/mbc.E18-04-0228

Acknowledgements

We thank P.D. Odermatt for help with refractive index measurements, and L. Labitigan for insightful discussions. This work was supported by the Howard Hughes Medical Institute. DV further acknowledges the Cancer Research Institute for support through a CRI Irvington fellowship. This work is partly supported by the US Department of Energy, Office of Basic Energy Science, under project DE-SC0010412 (YF and WC).

Author Contributions

D.V. and J.A.T. conceived of and designed the study. D.V. performed all experiments, wrote the image analysis software and analyzed the data. J.A.T. supervised the project. M.J.F. aided with the particle synthesis and conjugation and provided conjugated proteins. Y.W. and W.C. developed the elasticity theory, and performed the traction force calculations. D.V., Y.W., M.J.F., W.C. and J.A.T. wrote the paper.

Competing interests

D.V. , M.J.F. and J.A.T. have filed a provisional patent application based on the technology presented in this paper.

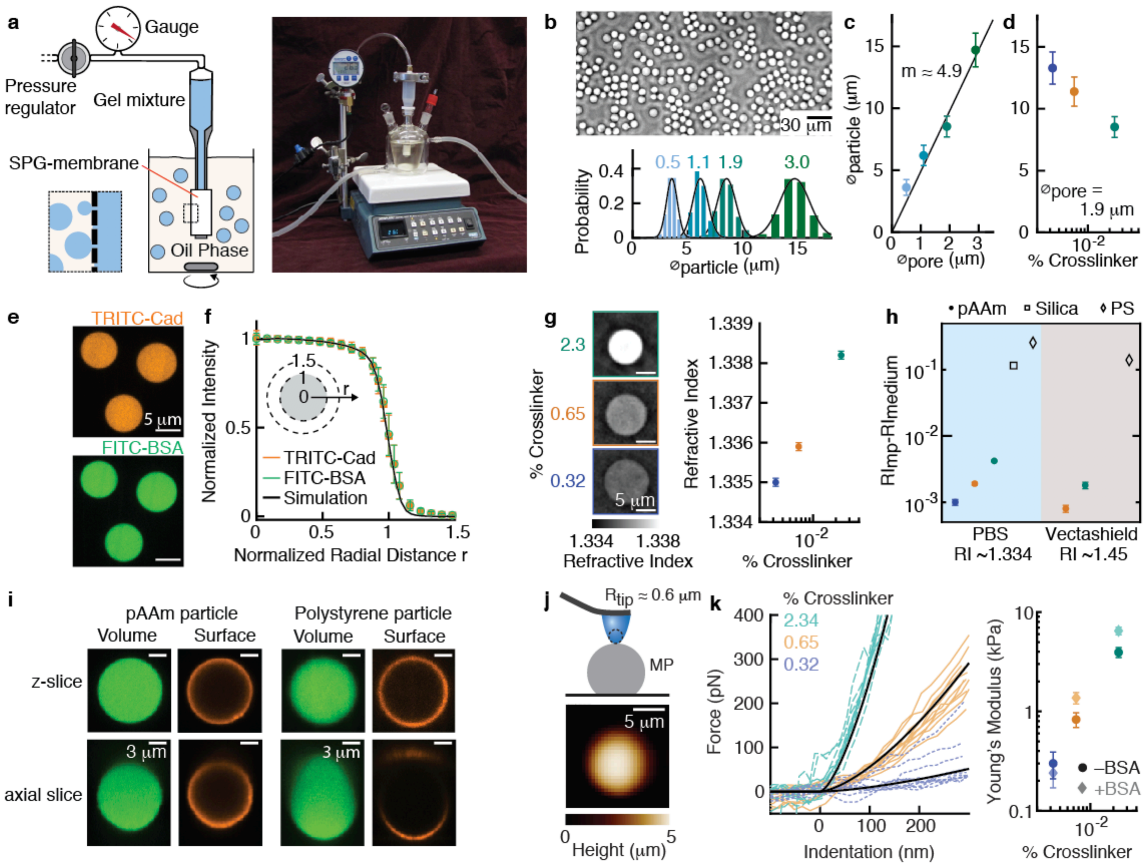

Figure 1: Characterization of batch-produced, easily conjugatable, deformable microparticles with cell-like mechanical properties. a, Schematic diagram and photograph of the essential components for membrane emulsification-based microparticle synthesis. **b,** (Top) Phase image of DAAM-particles obtained with 1.9 µm SPG membranes. (Bottom) Size distributions of DAAM-particles obtained with 0.5 – 3.0 µm SPG as quantified from phase images (n > 500 in each condition). Black lines represent Gaussian fits. **c,** Particle diameter dependence on membrane pore diameter, with the black line representing a linear fit through the origin. **d,** Quantification of particle size dependence on crosslinker concentration (n > 400 DAAM-particles in each condition). **e,** Confocal images (z-slices) of doubly functionalized DAAM-particles. **f,** Radial intensity profiles for C_c = 3.2%. >100 profiles were each normalized to intensity and radius, and then averaged. Black line indicates simulated data of a homogeneous sphere convolved with an experimentally determined PSF. **g,** (Left) Slices from 3D quantitative refractive index (*RI*) tomograms measured in PBS; (Right) quantification of *RI* in PBS (n = 7, 14, 28 DAAM-particles for C_c = 0.32%, 0.65% and 2.3%, respectively); **h,** *RI* difference between medium and particle in PBS and Vectashield (VS) (n = 9 & 12 for C_c = 0.65% & 2.3%, respectively). C_c = 0.32% in VS is missing because DAAM-particles were practically impossible to visualize, indicating a very close match in *RI*. Closed markers represent measurements, open markers (for polystyrene (PS) and silica) indicate specified values. Silica in VS is missing, as RI_{MP} - RI_{medium} ≈ 0. **i,** Z- and axial slices from representative confocal image stacks through a DAAM-particle (C_c = 0.32%) and a 10 µm Yellow-Green PS particle measured in PBS. DAAM-particles

were functionalized with Alexa 488-Cadaverine. Surface of DAAM-particles and PS MPs was functionalized with BSA, anti-BSA IgG, and immunostained with Alexa Fluor 546 secondary antibody. **j,** (Top) Schematic diagram of DAAM-particle mechanical characterization by AFM using large end-radius pyramidal tips. (Bottom) Typical AFM image of a DAAM-particle (C_c = 2.3%). **k,** (Left) Force-indentation curves (FDCs) on DAAM-particles functionalized with BSA (n = 11 DAAM-particles for each C_c). For each DAAM-particle, multiple indentation curves were made (2-5) and only the FDC closest to that particles' average behavior is visualized for clarity. (Right) Quantification of Young's moduli of DAAM-particles with and without BSA (n = 11, 14 & 12 for C_c = 0.32%, 0.65% and 3.2%, respectively). All error bars indicate standard deviations.

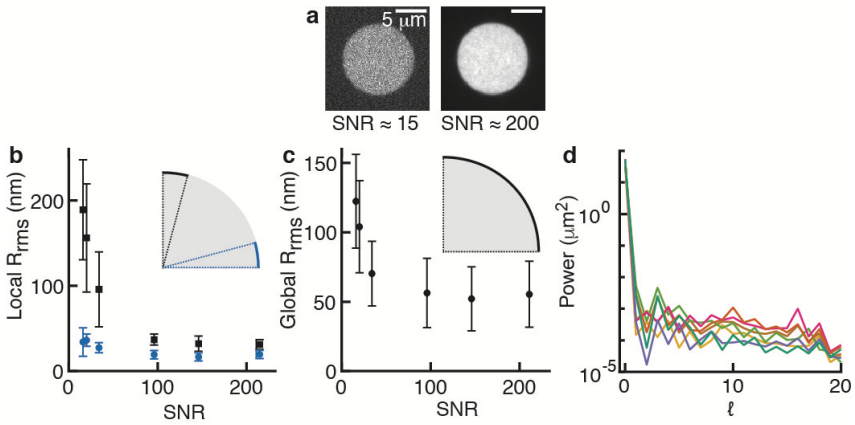

Figure 2: Superresolved edge localization and reference shape measurements of undeformed DAAM-particles. a. Confocal images (z-slices) of DAAM-particles taken with different laser power in Vectashield (VS) with different signal-to-noise ratios (SNR). SNR was calculated as $(\mu_{MP} - \mu_{bg})/s_{bg}$, where μ_{MP}, μ_{bg} are the mean fluorescent intensity of the particles and background, respectively, and s indicates the standard deviation of the background fluorescent intensity. **b.** Quantification of edge localization precision as the root-mean-squared surface roughness R_{rms} over a 1 μm^2 surface area (n = 7 DAAM-particles, the same set of particles is used for each condition). Localization precision near the equatorial plane (latitude < 15°) and at the upper apex (latitude > 75°), are visualized in blue and black, respectively. **c.** Surface roughness over the entire upper hemispheres (n = 7 DAAM-particles). **d.** Spherical harmonic power spectrum indicating the power of the distance to the centroid over the particle surface per degree ℓ (summed over orders m) for 7 particles; colours indicate individual particles.

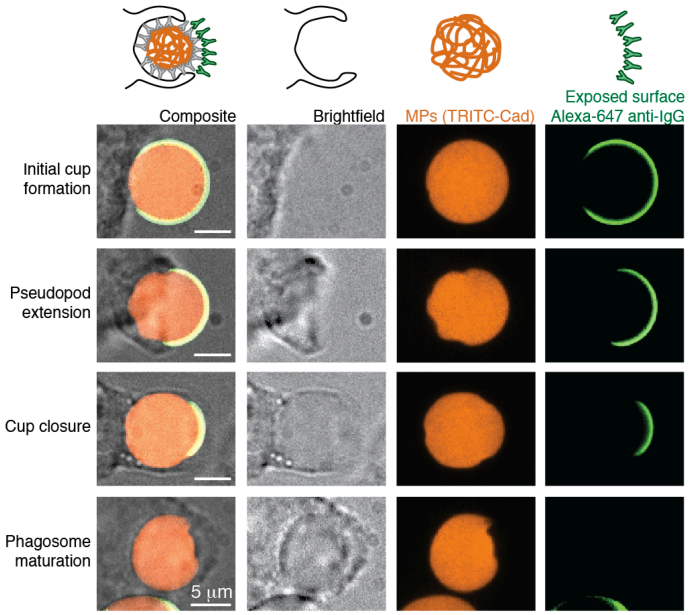

Figure 3: J774 macrophage-like cells deform DAAM-particles throughout IgG-mediated phagocytic engulfment. Confocal images (z-slices) through the centroid of particles undergoing phagocytosis. DAAM-particles were functionalized with TRITC-Cadaverine (Cad), BSA and anti-BSA IgG. J774 murine cells were exposed to DAAM-particles for 5 minutes and subsequently fixed. After fixation, the freely exposed particle surface was immunostained with Alexa-647 secondary antibody.

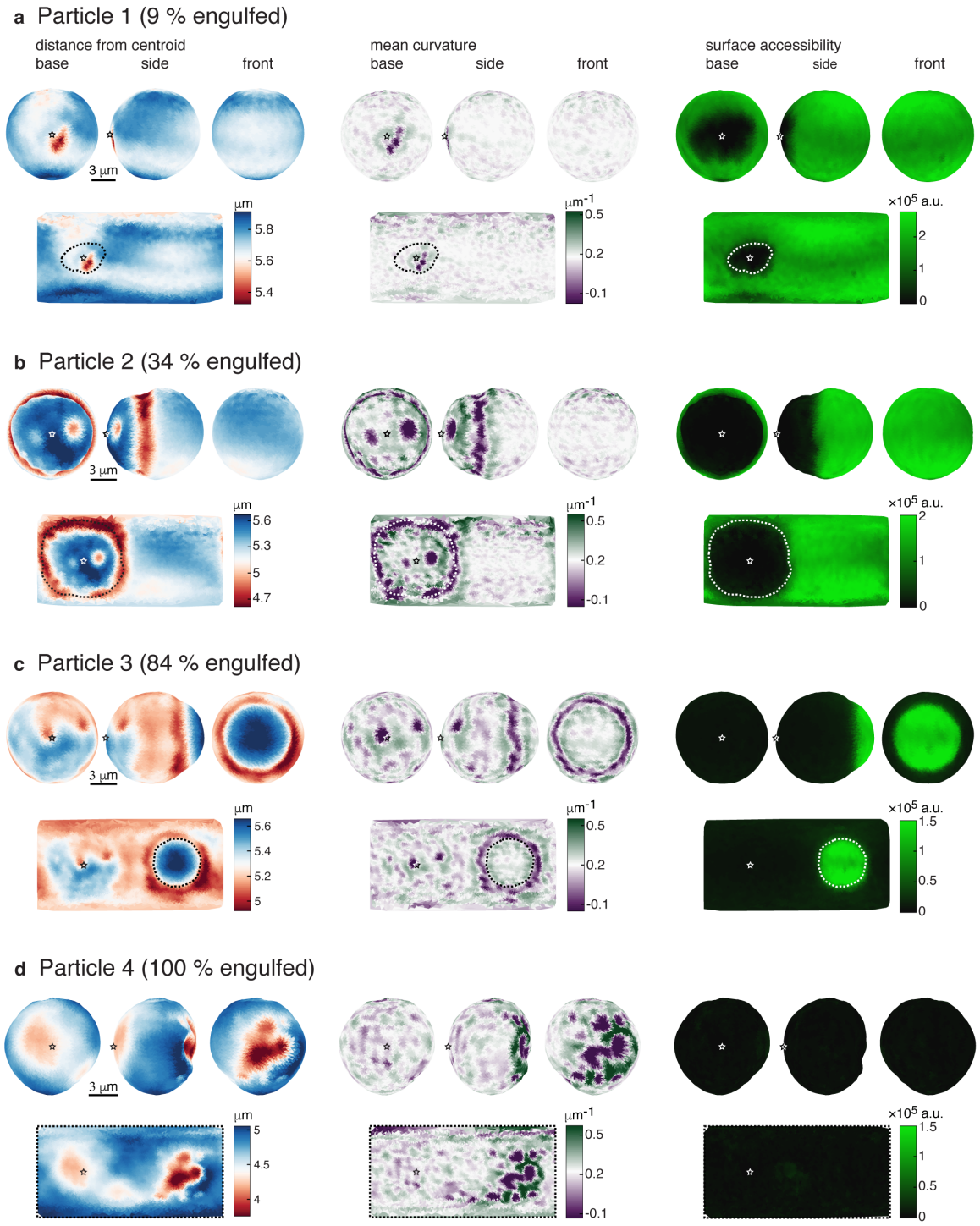

Figure 4: 3D reconstruction of model-targets deformed during phagocytic engulfment. a-d, Soft (C_c = 0.32%, E_y = 0.3 kPa) DAAM-particles imaged in various stages of phagocytic engulfment. Left, distance of the surface from the volumetric centroid. Middle, mean curvature of the particle surface. The colormap is centered around the median of the mean curvature (~1/R, with R the particle radius). Right, intensity signal (integrated along the radial direction) from immunostaining of the particle surface not in contact with the

cell. Top rows, visualization of particle surfaces from 3 different viewpoints. Bottom rows, Equirectangular map projections (standard parallel taken at latitude 0) showing the full particle surface, although necessarily distorted (most strongly around the polar regions). In these maps, the base of the phagocytic cup is visualized at latitude 0 and longitude $-\pi/2$. Stars (white or black) mark the base of the phagocytic cups (as determined from the binarized secondary antibody signal), and dashed lines (white or black) mark the outlines of the phagocytic cups.

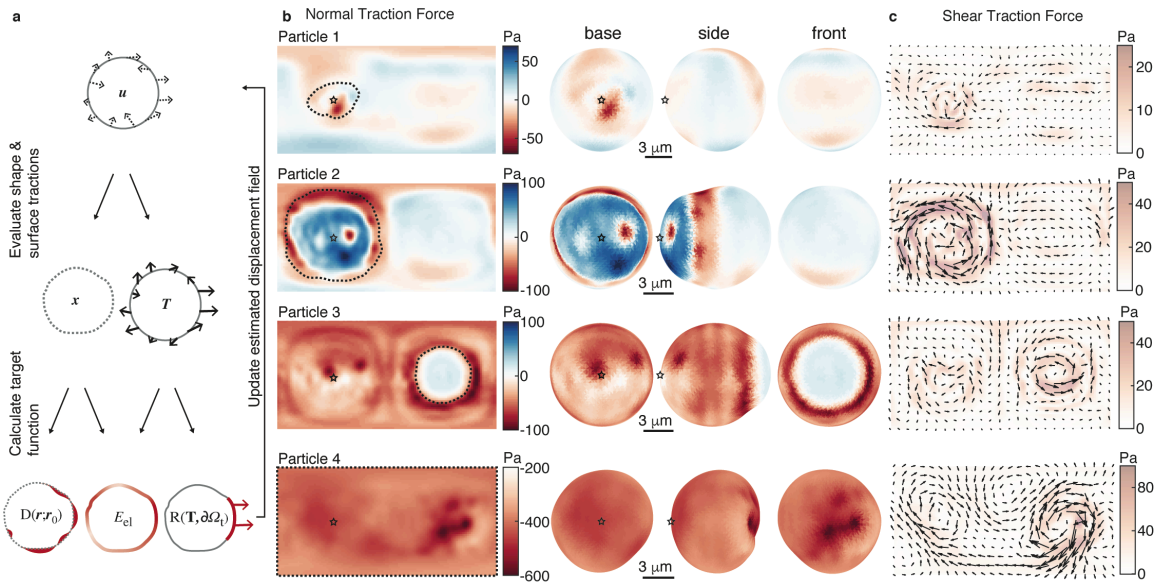

Figure 5: Direct computation of phagocytic traction forces from deformed particle shape. a, Schematic representation of the computational approach. The three elements of the cost function that are minimized for calculation of cellular forces are highlighted in red. Dashed arrow indicate the deformation field, whereas thick solid arrows indicate forces. **b,** Normal traction force reconstruction for soft DAAM-particles (C_c = 0.32%, E_y = 0.3 kPa) in various stages of engulfment. Left, equirectangular map projections (standard parallel taken at latitude 0) showing normal traction forces over the entire particle surface. The base of the phagocytic cup is visualized at latitude 0 and longitude –π/2. Right, visualization on the calculated particle shapes from 3 different viewpoints. Red color and negative values indicate inward compressive forces, whereas blue and positive values indicate outward tensile forces. **c,** Shear traction forces visualized in equirectangular map projections (similar as in b). Arrows indicate the direction of the shear forces. Black stars mark the base of the phagocytic cups (as determined from the binarized secondary antibody signal), and black dashed lines mark the outlines of the phagocytic cups. Tractions were calculated with spherical harmonic coefficients up to l_{max} = 20, and evaluated on a 21x41 grid. For visualization, the resulting forces were (up)sampled with 61x121 pixel density using the same set of spherical harmonic coefficients. Top to bottom, same four particles are shown as in figure 4.